Varatharajan, Anantaram; Pellegrino, Gianmario; Armando, Eric; Hinkkanen, Marko

Sensorless control of synchronous motor drives

Published in:
IEEE JOURNAL OF EMERGING AND SELECTED TOPICS IN POWER ELECTRONICS

DOI:
10.1109/JESTPE.2020.3037792

Published: 01/10/2021

Document Version
Peer-reviewed accepted author manuscript, also known as Final accepted manuscript or Post-print

Please cite the original version:
Varatharajan, A., Pellegrino, G., Armando, E., & Hinkkanen, M. (2021). Sensorless control of synchronous motor drives: Accurate torque estimation and control under parameter errors. *IEEE JOURNAL OF EMERGING AND SELECTED TOPICS IN POWER ELECTRONICS*, *9*(5), 5367-5376.
https://doi.org/10.1109/JESTPE.2020.3037792

Sensorless Control of Synchronous Motor Drives: Accurate Torque Estimation and Control under Parameter Errors

Anantaram Varatharajan, Gianmario Pellegrino, *Senior Member, IEEE,* Eric Armando, *Senior Member, IEEE,* and Marko Hinkkanen, *Senior Member, IEEE*

***Abstract*—Accurate torque control is of interest in traction and other industrial applications, whose realization is challenged by parameters errors and temperature induced variations. This paper proposes a sensorless technique for resilient torque control in salient synchronous machines. The position observer is driven by the adaptive projection vector for position error estimation (APP) scheme. A second projection vector, orthogonal to APP for non interference, serves for flux adaptation. Based on the torque estimation, a model-based optimal current reference generation for maximum torque per ampere (MTPA) condition is designed to realize accurate torque control. The proposed scheme is validated experimentally on an 1.1 kW synchronous reluctance (SyR) machine test-bench.**

***Index Terms*—Sensorless control, adaptive projection vector, flux adaptation, torque control, optimal current reference.**

I. Introduction

Control of synchronous machines without a position transducer finds importance in automotive and industrial applications for cost reduction and improved reliability. Low speed sensorless control techniques rely on high-frequency excitation approach to exploit the differential saliency for position estimation. This comprises of two schemes: continuous excitation using periodic signal injection [1] [2] and discontinuous excitation schemes [3]–[5]. In medium to high speed region, the high-frequency excitation approach is often relegated in favor of fundamental-wave excitation approach for reliability and low acoustic noise.

This paper concerns the latter category of fundamental-wave excitation methods based on back-emf integration for position estimation [6] [7]. An active flux based observer is a state of art technique reported in literature [8] [9] but suffers from instability at low speeds braking and at very high speeds motoring region as demonstrated in [10]–[12]. To circumvent instability, [10] proposed a flux observer with adaptive gain while [12] proposed an adaptive projection vector for position error estimation (APP) scheme. All such methods are parameter-dependent and suffers from parameter inaccuracy. The immunity property of the APP scheme to stator resistance variations and non-ideal inverter voltage compensation is illustrated in [13].

Another control aspect hampered by parameter inaccuracy is the torque estimation and control. Under parameter errors, the torque estimation is enhanced using inductance adaptation in extended back-emf based sensorless control of an interior permanent magnet synchronous motor (IPMSM) in [14]. However, due to the coupling of position observer with inductance adaption, a small residual error in torque estimation remains.

This paper presents a new torque control technique with maximum torque per ampere (MTPA) tracking and closed-loop compensation of torque estimation error caused by parameter inaccuracies, within the APP sensorless framework. The APP position observer can be supplemented with high-frequency excitation schemes for operation at zero to low speeds region [5]. Section II introduces notation and analysis of the flux observer. The APP scheme is elaborated in Section III along with the position observer. Section IV presents the main contributions of the paper, enumerated as follows:

1) An optimal current reference generation respecting MTPA criterion is devised as a function of discrepancy between commanded and estimated torque using the small-signal model of the machine.
2) An analytical expression for torque estimation error is derived as a function of parameter errors and steady-state position error. It is subsequently formulated for the APP sensorless scheme.
3) A projection vector that is orthogonal to APP is employed for current model flux adaptation, i.e., for correcting the error-prone flux-map. The orthogonality ensures decoupling and non-interference with the position observer.
4) The proposed adaptation of flux-map parameter errors is shown to alleviate the error in torque estimation. Thus, accurate torque control becomes realizable.
5) The stability analysis of the position observer with flux adaptation is reported in Section V.

Section VI presents the experimental validation of the proposed sensorless scheme with optimal torque control and flux adaptation on a 1.1 kW synchronous reluctance (SyR) machine test-bench. Finally, Section VII concludes the paper.

This work was supported by the Power Electronics Innovation Center (PEIC) of Politecnico di Torino, Italy. *(Corresponding author: Anantaram Varatharajan)*

A. Varatharajan, G. Pellegrino and E. Armando are with the Department of Energy, Politecnico di Torino, Turin 10129, Italy. (email: anantaram.varatharajan@polito.it; gianmario.pellegrino@polito.it; eric.armando@polito.it)

M. Hinkkanen is with the Department of Electrical Engineering and Automation, Aalto University, Espoo FI-00076, Finland (email: marko.hinkkanen@aalto.fi)

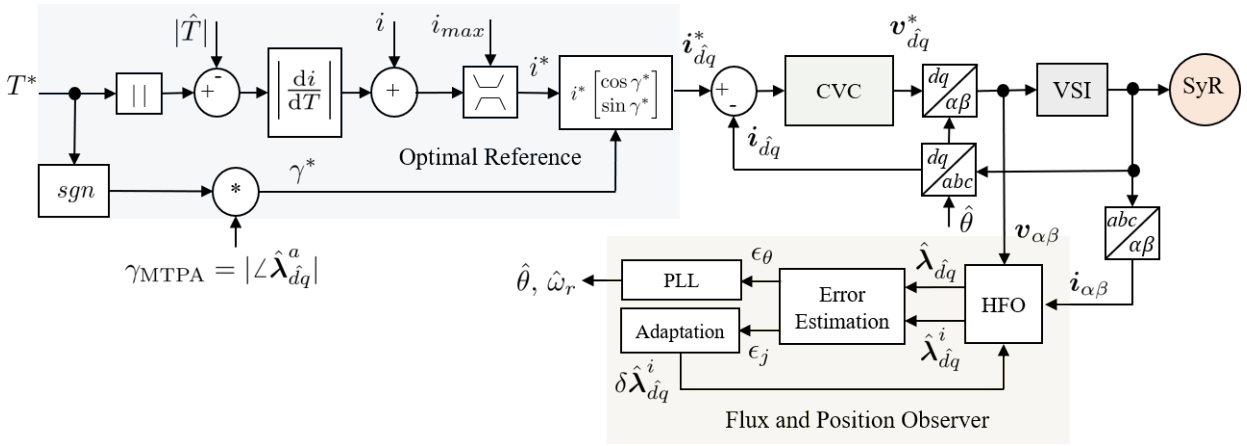

Fig. 1. Torque control system overview illustrating the model-based optimal current reference generation, hybrid flux observer (HFO) and position observer with flux adaptation.

II. Sensorless Control System

The electrical rotor position is θ and the electrical angular speed is $\omega = s\,\theta$ where s is the differential operator $\frac{\mathrm{d}}{\mathrm{d}t}$. Estimated vectors are represented by the superscript $\hat{}$. The orthogonal rotational matrix is $\mathbf{J} = \left[\begin{smallmatrix} 0 & -1 \\ 1 & 0 \end{smallmatrix}\right]$ and $\mathbf{I}$ is the identity matrix.

The machine model is expressed in coordinates of estimated rotor reference frame, denoted by subscript $\hat{dq}$, whose d-axis is at $\hat{\theta} = \theta - \tilde{\theta}$, where $\tilde{\theta}$ is the position error. Real space vectors will be used; for example, the stator current is $\boldsymbol{i}_{\hat{dq}} = [i_{\hat{d}}, i_{\hat{q}}]^{\mathrm{T}}$ where $i_{\hat{d}}$ and $i_{\hat{q}}$ are the vector components in estimated rotor reference frame. Space vectors in the stationary reference frame are denoted by subscript $\alpha\beta$. Note that the convention of a SyR machine is followed, i.e, d-axis is defined along the maximum inductance path. The block diagram illustrating an overview of the motor control is shown in Fig. 1.

A. Mathematical Model of a Synchronous Machine

The voltage equation of a synchronous machine in estimated rotor reference frame is expressed as

$$s\,\boldsymbol{\lambda}_{\hat{dq}} = \boldsymbol{v}_{\hat{dq}} - R_s \boldsymbol{i}_{\hat{dq}} - \hat{\omega}\,\mathbf{J}\,\boldsymbol{\lambda}_{\hat{dq}} \tag{1}$$

where R_s is the stator resistance and $\boldsymbol{\lambda}_{\hat{dq}}$ is the stator flux linkage. The electromagnetic torque is given by

$$T = \frac{3p}{2}\,\boldsymbol{i}_{\hat{dq}}^{\mathrm{T}}\,\mathbf{J}\,\boldsymbol{\lambda}_{\hat{dq}} \tag{2}$$

where p is the number of pole pairs.

Let $\boldsymbol{\Lambda}_{dq}(\boldsymbol{i}_{dq})$ denote the 2-D flux-map lookup tables of the machine under test, shown in Fig. 2, such that the actual flux in estimated reference frame is

$$\boldsymbol{\lambda}_{\hat{dq}} = \mathrm{e}^{\mathbf{J}\tilde{\theta}}\,\boldsymbol{\Lambda}_{dq}(\mathrm{e}^{-\mathbf{J}\tilde{\theta}}\,\boldsymbol{i}_{\hat{dq}}). \tag{3}$$

B. Hybrid Flux Observer

The flux observer is defined in the stationary reference frame as

$$s\hat{\boldsymbol{\lambda}}_{\alpha\beta} = \boldsymbol{v}_{\alpha\beta} - \hat{R}_s \boldsymbol{i}_{\alpha\beta} + \boldsymbol{G}_{\alpha\beta}\left(\mathrm{e}^{\mathbf{J}\hat{\theta}}\,\hat{\boldsymbol{\lambda}}^{i}_{\hat{dq}} - \hat{\boldsymbol{\lambda}}_{\alpha\beta}\right) \tag{4}$$

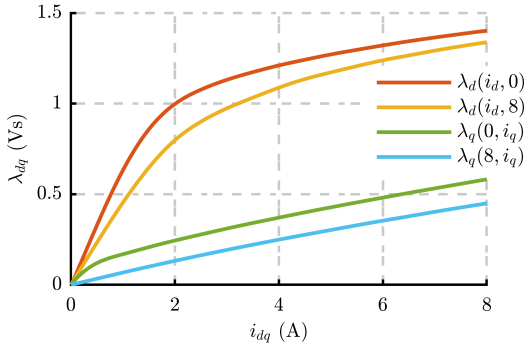

Fig. 2. Flux map of the SyR motor under test exhibiting saturation and cross-saturation characteristics. Experimentally identified with the constant speed test reported in [15].

where $\boldsymbol{G}_{\alpha\beta}$ is a 2×2 gain matrix, $\hat{\boldsymbol{\lambda}}^{i}_{\hat{dq}}$ is the current model flux estimate and $\hat{R}_s$ is the stator resistance used in the control. In estimated rotor reference frame, (4) transforms to

$$s\,\hat{\boldsymbol{\lambda}}_{\hat{dq}} = \boldsymbol{v}_{\hat{dq}} - \hat{R}_s \boldsymbol{i}_{\hat{dq}} - \hat{\omega}\mathbf{J}\,\hat{\boldsymbol{\lambda}}_{\hat{dq}} + \boldsymbol{G}\left(\hat{\boldsymbol{\lambda}}^{i}_{\hat{dq}} - \hat{\boldsymbol{\lambda}}_{\hat{dq}}\right) \tag{5}$$

where the gain matrix $\boldsymbol{G}$ is given by

$$\boldsymbol{G} = \mathrm{e}^{-\mathbf{J}\hat{\theta}}\,\boldsymbol{G}_{\alpha\beta}\,\mathrm{e}^{\mathbf{J}\hat{\theta}}. \tag{6}$$

In this work, a diagonal matrix $\boldsymbol{G} = g\,\mathbf{I}$ is used; hence, the equivalence $\boldsymbol{G} = \boldsymbol{G}_{\alpha\beta}$ holds. The gain g dictates the dominance of the current model on the flux observer; for electrical speeds above g rad/s, the voltage model [back-emf integration in (1)] prevails. Hence, for speeds below g, it is recommended to switch to the high-frequency excitation based sensorless schemes. The observer is called hybrid to signify the combination of voltage and current models.

C. Linearized Error Dynamics

To aid in further analysis, the nonlinear flux estimation error dynamics is derived from (1) and (5) as

$$s\,\tilde{\boldsymbol{\lambda}}_{\hat{dq}} = -(\boldsymbol{G} + \hat{\omega}\mathbf{J})\,\tilde{\boldsymbol{\lambda}}_{\hat{dq}} + \boldsymbol{G}\,(\boldsymbol{\lambda}_{\hat{dq}} - \hat{\boldsymbol{\lambda}}^{i}_{\hat{dq}}) - \tilde{R}_s \boldsymbol{i}_{\hat{dq}} \tag{7}$$

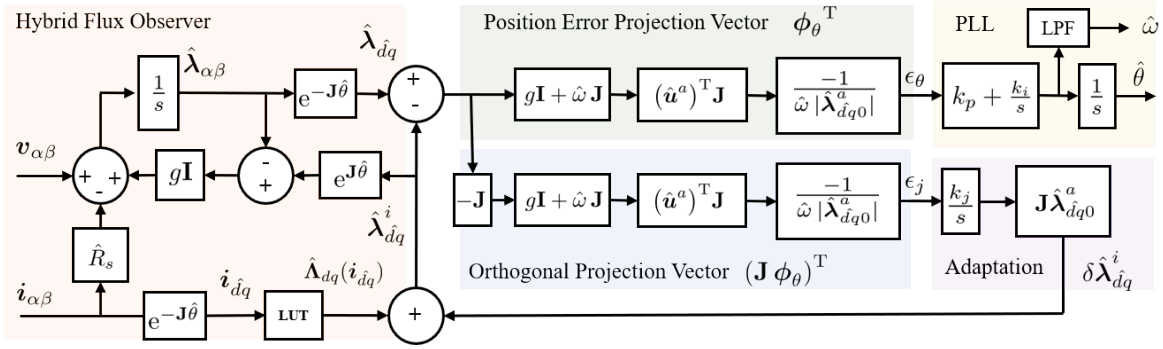

Fig. 3. Hybrid flux observer in stator reference frame with the APP position observer augmented with flux adaptation for accurate torque estimation.

where $\tilde{\boldsymbol{\lambda}}_{\hat{dq}} = \boldsymbol{\lambda}_{\hat{dq}} - \hat{\boldsymbol{\lambda}}_{\hat{dq}}$ is the flux estimation error and $\tilde{R}_s = R_s - \hat{R}_s$ is the error in temperature-dependent stator resistance.

Let $\hat{\boldsymbol{\Lambda}}_{dq}(\boldsymbol{i}_{dq})$ denote the estimated flux-map carrying parameter errors characterized as

$$\tilde{\boldsymbol{\lambda}}^{i}_{\hat{dq}} = \boldsymbol{\Lambda}_{dq}(\boldsymbol{i}_{\hat{dq}}) - \hat{\boldsymbol{\Lambda}}_{dq}(\boldsymbol{i}_{\hat{dq}}). \tag{8}$$

Then, the discrepancy between the actual flux (3) and the current model flux estimates, $\boldsymbol{\lambda}_{\hat{dq}} - \hat{\boldsymbol{\lambda}}^{i}_{\hat{dq}}$, can be expressed as

$$\boldsymbol{\lambda}_{\hat{dq}} - \hat{\boldsymbol{\lambda}}^{i}_{\hat{dq}} = \mathrm{e}^{\mathbf{J}\tilde{\theta}}\, \boldsymbol{\Lambda}_{dq}(\mathrm{e}^{-\mathbf{J}\tilde{\theta}}\, \boldsymbol{i}_{\hat{dq}}) - \hat{\boldsymbol{\Lambda}}_{dq}(\boldsymbol{i}_{\hat{dq}}). \tag{9}$$

Linearizing the term $\boldsymbol{\Lambda}_{dq}(\mathrm{e}^{-\mathbf{J}\tilde{\theta}}\, \boldsymbol{i}_{\hat{dq}})$ around an operating point, marked by a subscript 0, gives

$$\boldsymbol{\Lambda}_{dq}(\mathrm{e}^{-\mathbf{J}\tilde{\theta}}\, \boldsymbol{i}_{\hat{dq}}) = \boldsymbol{\Lambda}_{dq}(\boldsymbol{i}_{\hat{dq}0}) - \frac{\partial \boldsymbol{\Lambda}_{dq}}{\partial \boldsymbol{i}_{\hat{dq}}}\Big|_{\boldsymbol{i}_{\hat{dq}0}} \mathbf{J}\, \boldsymbol{i}_{\hat{dq}0}\, \tilde{\theta}. \tag{10}$$

The incremental inductance matrix $\boldsymbol{L}_{\partial}$ is defined as

$$\boldsymbol{L}_{\partial} = \frac{\partial \boldsymbol{\lambda}_{dq}}{\partial \boldsymbol{i}_{dq}} = \begin{bmatrix} l_d & l_{dq} \\ l_{dq} & l_q \end{bmatrix} \tag{11}$$

where l_d, l_q represents the incremental inductance along direct d and quadrature q axis, respectively, while l_{dq} is the cross-saturation term. All quantities are functions of $\boldsymbol{i}_{dq}$. With $\mathrm{e}^{-\mathbf{J}\tilde{\theta}} = 1 - \tilde{\theta}\mathbf{J}$ and excluding the higher order terms, the expression (9) becomes

$$\boldsymbol{\lambda}_{\hat{dq}} - \hat{\boldsymbol{\lambda}}^{i}_{\hat{dq}} \approx \left[\mathbf{J}\, \hat{\boldsymbol{\Lambda}}_{dq}(\boldsymbol{i}_{\hat{dq}0}) - \boldsymbol{L}_{\partial}\, \mathbf{J}\, \boldsymbol{i}_{\hat{dq}0}\right] \tilde{\theta} + \tilde{\boldsymbol{\lambda}}^{i}_{\hat{dq}}. \tag{12}$$

The coefficient of position error in (12) is defined as the auxiliary flux vector, given by

$$\hat{\boldsymbol{\lambda}}^{a}_{\hat{dq}0} = \mathbf{J}\, \hat{\boldsymbol{\lambda}}^{i}_{\hat{dq}0} - \boldsymbol{L}_{\partial}\, \mathbf{J}\, \boldsymbol{i}_{\hat{dq}0}. \tag{13}$$

Finally, the expression (9) simplifies to

$$\boldsymbol{\lambda}_{\hat{dq}} - \hat{\boldsymbol{\lambda}}^{i}_{\hat{dq}} = \hat{\boldsymbol{\lambda}}^{a}_{\hat{dq}0}\, \tilde{\theta} + \tilde{\boldsymbol{\lambda}}^{i}_{\hat{dq}}. \tag{14}$$

Thus, the linearized flux estimation error dynamics as functions of errors in position, resistance and current model flux is derived as

$$\tilde{\boldsymbol{\lambda}}_{\hat{dq}} = (s\mathbf{I} + \boldsymbol{G} + \omega_0 \mathbf{J})^{-1} \left[\boldsymbol{G}\, (\hat{\boldsymbol{\lambda}}^{a}_{\hat{dq}0}\, \tilde{\theta} + \tilde{\boldsymbol{\lambda}}^{i}_{\hat{dq}}) - \tilde{R}_s \boldsymbol{i}_{\hat{dq}0}\right]. \tag{15}$$

This will be used in Section III to formulate the position error signal and in Section IV to express the torque estimation error.

D. Projection Vector Framework

The error signal ϵ driving the observer adaptation law is expressed in general form as the projection of the difference in observed and current model flux estimates on a projection vector $\boldsymbol{\phi}$, according to [10] [12], as

$$\epsilon = \boldsymbol{\phi}^{\mathrm{T}}\, (\hat{\boldsymbol{\lambda}}_{\hat{dq}} - \hat{\boldsymbol{\lambda}}^{i}_{\hat{dq}}). \tag{16}$$

This will be used for position tracking and current model flux adaptation. Using flux estimation error $\tilde{\boldsymbol{\lambda}}_{\hat{dq}} = \boldsymbol{\lambda}_{\hat{dq}} - \hat{\boldsymbol{\lambda}}_{\hat{dq}}$ and (14), the linearized form of (16) becomes

$$\epsilon = \boldsymbol{\phi}^{\mathrm{T}}\, \big(\hat{\boldsymbol{\lambda}}^{a}_{\hat{dq}0}\, \tilde{\theta} + \tilde{\boldsymbol{\lambda}}^{i}_{\hat{dq}} - \tilde{\boldsymbol{\lambda}}_{\hat{dq}}\big). \tag{17}$$

Following the results of flux estimation error dynamics (15), the error signal (17) is decomposed in terms of the constituent errors as

$$\epsilon = \boldsymbol{\phi}^{\mathrm{T}} \begin{bmatrix} \boldsymbol{h}_{\tilde{\theta}} & \boldsymbol{H}_{\tilde{\boldsymbol{\lambda}}^{i}} & \boldsymbol{h}_{\tilde{R}} \end{bmatrix} \tilde{\boldsymbol{y}} \tag{18a}$$

$$\begin{aligned} \boldsymbol{h}_{\tilde{\theta}} &= (s\mathbf{I} + \boldsymbol{G} + \omega_0 \mathbf{J})^{-1} (s\mathbf{I} + \omega_0 \mathbf{J})\, \hat{\boldsymbol{\lambda}}^{a}_{\hat{dq}0} \\ \boldsymbol{H}_{\tilde{\boldsymbol{\lambda}}^{i}} &= (s\mathbf{I} + \boldsymbol{G} + \omega_0 \mathbf{J})^{-1} (s\mathbf{I} + \omega_0 \mathbf{J}) \\ \boldsymbol{h}_{\tilde{R}} &= (s\mathbf{I} + \boldsymbol{G} + \omega_0 \mathbf{J})^{-1}\, \boldsymbol{i}_{\hat{dq}0} \end{aligned} \tag{18b}$$

where $\tilde{\boldsymbol{y}} = \begin{bmatrix} \tilde{\theta} & (\tilde{\boldsymbol{\lambda}}^{i}_{\hat{dq}})^{\mathrm{T}} & \tilde{R}_s \end{bmatrix}^{\mathrm{T}}$. The transfer function matrices $\boldsymbol{h}_{\tilde{\theta}}$ and $\boldsymbol{h}_{\tilde{R}}$ are of length 2×1 while $\boldsymbol{H}_{\tilde{\boldsymbol{\lambda}}^{i}}$ is 2×2.

III. APP Position Observer

This section briefly reviews the APP scheme proposed in [12]. The framework developed will be used in Section IV for accurate torque estimation and control. The block diagram of the proposed position observer with current model flux adaptation is shown in Fig. 3.

A. APP Projection Vector

Let ϵ_θ denote the position error signal. In the absence of parametric errors, the position error projection vector $\boldsymbol{\phi}_\theta$ is designed to hold the equality between position error signal and position error, barring dynamics as

$$\epsilon_\theta\big|_{s=0} = \boldsymbol{\phi}_\theta^{\mathrm{T}}\, (\hat{\boldsymbol{\lambda}}_{\hat{dq}} - \hat{\boldsymbol{\lambda}}^{i}_{\hat{dq}})\big|_{s=0} = \tilde{\theta}. \tag{19}$$

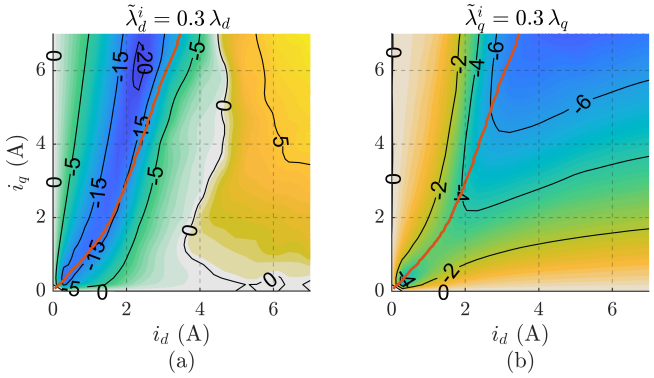

Fig. 4. Steady-state position error $\tilde{\theta}_0$ in degrees (electrical): (a) +30% error in d-axis, $\tilde{\lambda}_d^i = 0.3\,\lambda_d$; (b) +30 % error in q-axis, $\tilde{\lambda}_q^i = 0.3\,\lambda_q$. In red is the MTPA trajectory.

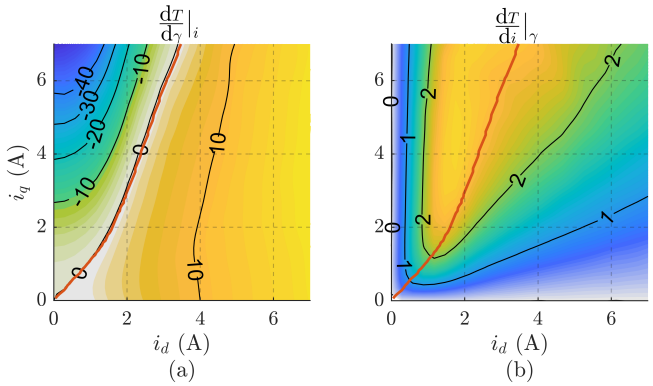

Fig. 5. (a) Contour of derivative of torque w.r.t current angle in (27) for MTPA adaptation; (b) Contour of derivative of torque w.r.t current amplitude in (31) for reference torque tracking. Red curve is the MTPA trajectory.

The equality (19) is satisfied when $\boldsymbol{\phi}_\theta^{\mathrm{T}}\,\boldsymbol{h}_{\tilde{\theta}}\big|_{s=0} = 1$; from (18), this leads to a projection vector of nature

$$\boldsymbol{\phi}_\theta^{\mathrm{T}} = \frac{-1}{\omega_0\,|\hat{\boldsymbol{\lambda}}_{\hat{d}q0}^{a}|}\,\big(\hat{\boldsymbol{u}}^a\big)^{\mathrm{T}}\,\mathbf{J}\,\big(\boldsymbol{G} + \omega_0\,\mathbf{J}\big). \tag{20}$$

where $\hat{\boldsymbol{u}}^a$ is an unit vector along the auxiliary flux vector as

$$\hat{\boldsymbol{u}}^a = \frac{\hat{\boldsymbol{\lambda}}_{\hat{d}q0}^{a}}{|\hat{\boldsymbol{\lambda}}_{\hat{d}q0}^{a}|}. \tag{21}$$

B. Speed and Position Observer

A conventional phase lock loop (PLL) with a proportional-integral (PI) controller is employed to drive the position error signal ϵ_θ to zero as

$$\hat{\omega} = k_p\,\epsilon_\theta + \omega_i \qquad \omega_i = \int k_i\,\epsilon_\theta\,\mathrm{d}t \qquad \hat{\theta} = \int \hat{\omega}\,\mathrm{d}t \tag{22}$$

where k_p and k_i are the respective gains. The gains of the PLL are tuned for a critically damped response considering $\epsilon_\theta = \tilde{\theta}$ by placing the two poles at $s = -\Omega_\omega$:

$$k_p = 2\,\Omega_\omega \qquad k_i = \Omega_\omega^2. \tag{23}$$

For the PLL defined in (22), the closed loop transfer function is given by

$$\frac{\hat{\theta}(s)}{\theta(s)} = \frac{(sk_p + k_i)\,\boldsymbol{\phi}_\theta^{\mathrm{T}}\,\boldsymbol{h}_{\tilde{\theta}}}{s^2 + (sk_p + k_i)\,\boldsymbol{\phi}_\theta^{\mathrm{T}}\,\boldsymbol{h}_{\tilde{\theta}}} \tag{24}$$

where the transfer function between the position error signal and position error for the projection vector (20) is derived from (18) as

$$\boldsymbol{\phi}_\theta^{\mathrm{T}}\,\boldsymbol{h}_{\tilde{\theta}} = \frac{\epsilon_\theta}{\tilde{\theta}} = \frac{s^2 + sg + g^2 + \omega_0^2}{(s+g)^2 + \omega_0^2}. \tag{25}$$

The transfer function (25) is observed to be independent of the operating point $\boldsymbol{i}_{dq0}$ and the sign of rotation. It can be inferred that the steady-state gain $\boldsymbol{\phi}_\theta^{\mathrm{T}}\,\boldsymbol{h}_{\tilde{\theta}}\big|_{s=0} = 1$. The stability is evaluated from the frequency response plot of the closed loop transfer function (24) in [13].

C. Sensitivity to Parameter Errors

Under parameter errors, the steady-state position error $\tilde{\theta}_0$ is determined using the projection vector (20) in the linearized model (18) at $\epsilon_\theta = 0$ as

$$\tilde{\theta}_0 = \frac{-1}{|\hat{\boldsymbol{\lambda}}_{\hat{d}q0}^{a}|}\,\big(\hat{\boldsymbol{u}}^a\big)^{\mathrm{T}}\,\tilde{\boldsymbol{\lambda}}_{\hat{d}q0}^{i} + \frac{\tilde{R}_s}{\omega_0\,|\hat{\boldsymbol{\lambda}}_{\hat{d}q0}^{a}|}\,\big(\hat{\boldsymbol{u}}^a\big)^{\mathrm{T}}\,\mathbf{J}\,\boldsymbol{i}_{\hat{d}q0}. \tag{26}$$

It is to be noted that (26) may not hold for large parameter errors since it is based on the linearized model. It can be observed that the coefficient of $\tilde{R}_s$ resembles the MTPA law definition (28) defined later in Section IV-A; this relates to the resistance immunity property of APP along the MTPA trajectory as reported in [13].

It is discerned from (26) that the steady-state position error is dependent on the parameter error in the direction along the auxiliary flux vector. The steady-state position error due to +30% error in d and q-axes flux-map, separately considered, is shown in Figs. 4(a) and 4(b) respectively. The steady-state position error in Fig. 4(a) is approximately 15° along the MTPA trajectory while in Fig. 4(b), it is approximately 4° at the rated torque. The control is more susceptible to d-axis due to the relatively large error in absolute value, i.e., $\tilde{\lambda}_d > \tilde{\lambda}_q$.

IV. Proposed MTPA Control Scheme

This Section presents the new model-based torque control scheme and the current model flux adaptation for accurate torque estimation under parameter errors.

A. MTPA Law

Let γ denote the current angle. The change of torque w.r.t current angle for a given current amplitude $i = |\boldsymbol{i}_{dq}|$ is computed as

$$\begin{aligned}\frac{\mathrm{d}T}{\mathrm{d}\gamma}\Big|_i &= \frac{3p}{2}\left(\frac{\mathrm{d}\boldsymbol{i}_{dq}}{\mathrm{d}\gamma}^{\mathrm{T}}\,\mathbf{J}\,\boldsymbol{\lambda}_{dq} + \boldsymbol{i}_{dq}^{\mathrm{T}}\,\mathbf{J}\,\frac{\mathrm{d}\boldsymbol{\lambda}_{dq}}{\mathrm{d}\gamma}\right)\\ &= \frac{3p}{2}\left(\mathbf{J}\,\boldsymbol{\lambda}_{dq} - \boldsymbol{L}_\partial\,\mathbf{J}\,\boldsymbol{i}_{dq}\right)^{\mathrm{T}}\,\mathbf{J}\,\boldsymbol{i}_{dq}.\end{aligned} \tag{27}$$

The contour of (27) for machine under test is shown in Fig. 5(a) where the zero locus is observed to be coincident with the MTPA trajectory. Using the auxiliary flux vector (13), the MTPA law is defined as

$$\frac{\mathrm{d}T}{\mathrm{d}\gamma}\Big|_i = 0 \quad \Rightarrow \quad \frac{3p}{2}\left(\boldsymbol{\lambda}^a_{dq}\right)^{\mathrm{T}} \mathbf{J}\, \boldsymbol{i}_{dq} = 0. \tag{28}$$

The expression (28) dictates that the MTPA criterion is respected *if and only if* the stator current is in phase with the auxiliary flux vector, i.e., $\gamma_{\mathrm{MTPA}} = \angle \boldsymbol{\lambda}^a_{dq}$.

B. Optimal Current Reference Computation

For the commanded torque reference T^*, the current reference magnitude i^* is analytically derived as

$$i^* = i + \Big|\frac{\mathrm{d}i}{\mathrm{d}T}\Big|_\gamma \cdot \left(|T^*| - |\hat{T}|\right) \tag{29}$$

where the estimated torque $\hat{T}$ is computed with the observed flux in the torque equation (2). The derivative of torque w.r.t current amplitude for a given current angle can be expressed in dq reference frame as

$$\frac{\mathrm{d}T}{\mathrm{d}i}\Big|_\gamma = \frac{3p}{2}\left(\frac{\boldsymbol{i}^{\mathrm{T}}_{dq}}{i}\mathbf{J}\,\boldsymbol{\lambda}_{dq} + \boldsymbol{i}^{\mathrm{T}}_{dq}\mathbf{J}\,\boldsymbol{L}_\partial\,\frac{\boldsymbol{i}_{dq}}{i}\right). \tag{30}$$

Upon manipulation,

$$\frac{\mathrm{d}T}{\mathrm{d}i}\Big|_\gamma = \frac{3p}{2}\,\frac{\boldsymbol{i}^{\mathrm{T}}_{dq}}{i}\,\mathbf{J}\left(\boldsymbol{\lambda}_{dq} + \boldsymbol{L}_\partial\,\boldsymbol{i}_{dq}\right). \tag{31}$$

The contours of (31) for the machine under test is shown in Fig. 5(b). These are representative of the torque factor (Nm/A), being maximum along the MTPA trajectory shown in red. Note that care must be taken at very low loads as the quantity in (31) approaches zero at either axes as seen in Fig. 5(b): otherwise said, the SyR machine cannot produce torque without current excitation in both the axes.

The inverse of the quantity (31) can be real-time computed using the measured current angle, the observed flux and the incremental inductances retrieved from flux-map, all in estimated coordinates.

Finally, the optimal reference current is computed as

$$\boldsymbol{i}^*_{\hat{dq}} = i^* \begin{bmatrix}\cos\gamma^* \\ \sin\gamma^*\end{bmatrix}. \tag{32}$$

The reference current angle magnitude is determined by the MTPA criterion, $|\gamma^*| = |\gamma_{\mathrm{MTPA}}|$ and it takes the sign of T^*, as shown in Fig. 1.

C. Torque Estimation Error

The parameter dependent position error (26) and the direct effect of parameter errors contribute to the torque estimation error. This directly translates to the error in torque output w.r.t commanded torque through (29). The steady-state error of the estimated electromagnetic torque $\tilde{T}_0$ is given by

$$\tilde{T}_0 = \frac{3p}{2}\,\boldsymbol{i}^{\mathrm{T}}_{\hat{dq}0}\,\mathbf{J}\,\tilde{\boldsymbol{\lambda}}_{\hat{dq}0}. \tag{33}$$

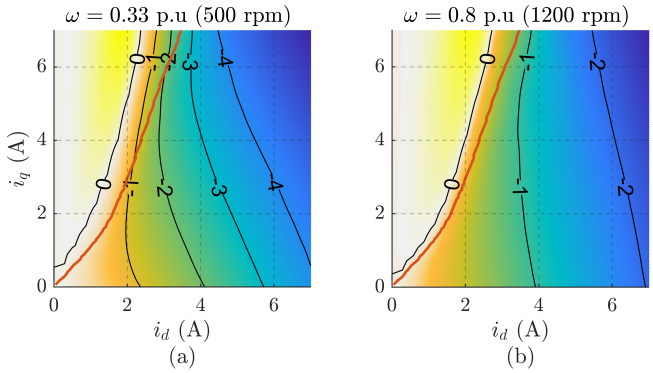

Fig. 6. Steady-state torque estimation error $\tilde{T}_0$ in Nm at +30% error in d-axis, $\tilde{\lambda}^i_d = 0.3\,\lambda_d$: (a) $\omega = 0.33$ p.u. (500 rpm); (b) $\omega = 0.8$ p.u. (1200 rpm). In red is the MTPA trajectory. Rated torque $T_n = 7.1$ Nm; $g = 2\,\pi \cdot 10$ rad/s.

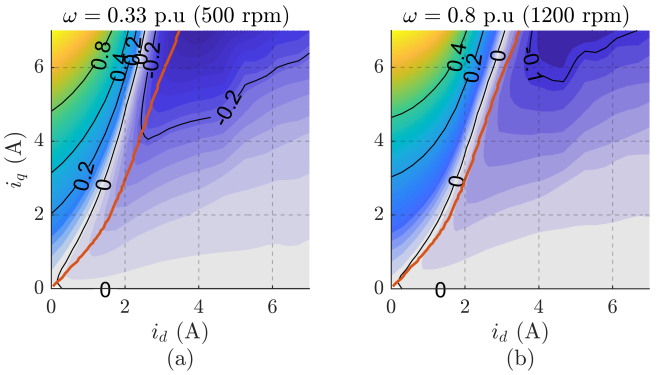

Fig. 7. Steady-state torque estimation error $\tilde{T}_0$ in Nm at +30% error in q-axis, $\tilde{\lambda}^i_q = 0.3\,\lambda_q$: (a) $\omega = 0.33$ p.u. (500 rpm); (b) $\omega = 0.8$ p.u. (1200 rpm). In red is the MTPA trajectory. Rated torque $T_n = 7.1$ Nm; $g = 2\,\pi \cdot 10$ rad/s.

Using the steady-state flux estimation error, $s = 0$ in (15), the torque estimation error becomes

$$\tilde{T}_0 = \frac{3p}{2}\,\boldsymbol{i}^{\mathrm{T}}_{\hat{dq}0}\,\mathbf{J}\left(\boldsymbol{G} + \omega_0\mathbf{J}\right)^{-1}\left[\boldsymbol{G}\left(\hat{\boldsymbol{\lambda}}^a_{\hat{dq}0}\,\tilde{\theta}_0 + \tilde{\boldsymbol{\lambda}}^i_{\hat{dq}}\right) - \tilde{R}_s\boldsymbol{i}_{\hat{dq}0}\right]. \tag{34}$$

Substituting position error (26) into (34) and considering accurate stator resistance, the terms in phase with the auxiliary flux vector cancel out and the torque estimation error simplifies to

$$\tilde{T}_0 = \frac{3p}{2}\,\boldsymbol{i}^{\mathrm{T}}_{\hat{dq}0}\,\mathbf{J}\left(\boldsymbol{G} + \omega_0\mathbf{J}\right)^{-1}\boldsymbol{G}\,\mathbf{J}\,\hat{\boldsymbol{u}}^a \cdot \left(\mathbf{J}\,\hat{\boldsymbol{u}}^a\right)^{\mathrm{T}}\tilde{\boldsymbol{\lambda}}^i_{\hat{dq}}. \tag{35}$$

The expression (35) states that the torque estimation error is a function of the operating speed and is proportional to the current model flux error orthogonal to auxiliary flux vector, i.e., $\mathbf{J}\,\hat{\boldsymbol{u}}^a$.

The steady-state torque estimation error contour (35) for +30% errors in the d-axis flux-map ($\tilde{\lambda}^i_d = 0.3\,\lambda_d$) at speeds $\omega = 0.33$ p.u. and $\omega = 0.8$ p.u.. is shown in Figs. 6(a) and 6(b), respectively. The same plots are reproduced for +30% errors in the q-axis flux-map ($\tilde{\lambda}^i_q = 0.3\,\lambda_q$) in Fig. 7. It is observed that the torque error is more sensitive to the d-axis parameter error and the estimation accuracy degrades with decreasing speed.

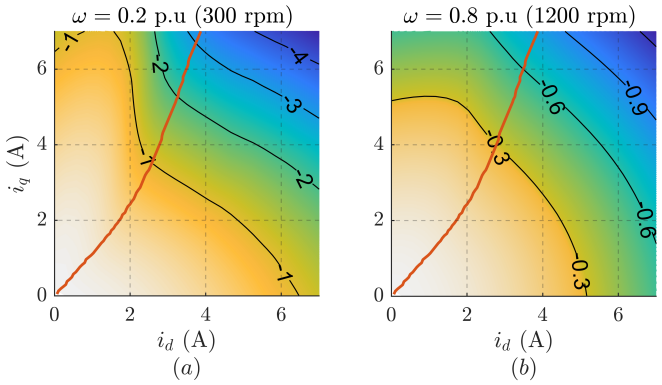

Fig. 8. Steady-state torque estimation error $\tilde{T}_0$ in Nm at $\tilde{R}_s = 1\Omega$ (0.16 p.u.): (a) $\omega = 0.2$ p.u. (300 rpm); (b) $\omega = 0.8$ p.u. (1200 rpm). In red is the MTPA trajectory. Rated torque $T_n = 7.1$ Nm; $g = 2\,\pi \cdot 10$ rad/s.

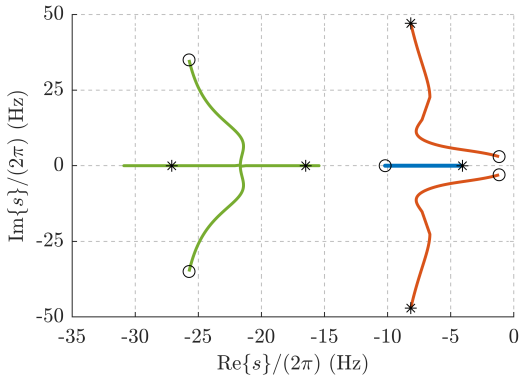

Fig. 9. Locus of poles of the position observer with flux adaptation for $\omega = 0.1 \ldots 1$ p.u. at rated $T = 7.1$ Nm (MTPA) where the markers $\circ$ and $*$ denote the speeds 0.1 and 1 p.u., respectively. Color code: PLL poles are denoted in green, flux observer in red, current model flux adaptation in blue.

D. Current Model Flux Adaptation

Exploiting the two degrees of freedom of the error domain in (16), a second projection vector orthogonal to APP $(\mathbf{J}\,\boldsymbol{\phi}_\theta)$ can be utilized to adapt flux-map. In [13], the feasibility of the stator resistance and the inductance adaptation were investigated. However, adapting a single parameter (eg. d-axis inductance) in the presence of flux-map error in both d and q-axes introduces coupling and could, in some cases, negatively influence the position observer.

A new flux adaptation law is developed to be decoupled and independent of the position observer. To this end, the error signal ϵ_j for flux adaptation is given by

$$\epsilon_j = \left(\mathbf{J}\,\boldsymbol{\phi}_\theta\right)^{\mathrm{T}} \left(\hat{\boldsymbol{\lambda}}_{\hat{d}q} - \hat{\boldsymbol{\lambda}}^{i}_{\hat{d}q}\right). \tag{36}$$

Owing to the orthogonality, it follows from (18) that the error signal (36) is independent of the position error, barring the dynamics, as

$$\left(\mathbf{J}\,\boldsymbol{\phi}_\theta\right)^{\mathrm{T}} \boldsymbol{h}_{\tilde{\theta}}\big|_{s=0} = 0. \tag{37}$$

The feasibility of current model flux adaptation is examined using the transfer function matrix $\boldsymbol{H}_{\tilde{\boldsymbol{\lambda}}^i}$ in (18b) as

$$\left(\mathbf{J}\,\boldsymbol{\phi}_\theta\right)^{\mathrm{T}} \boldsymbol{H}_{\tilde{\boldsymbol{\lambda}}^i}\big|_{s=0} = \frac{1}{|\hat{\boldsymbol{\lambda}}^{a}_{\hat{d}q0}|} \left(\mathbf{J}\,\hat{\boldsymbol{u}}^a\right)^{\mathrm{T}}. \tag{38}$$

The expression (38) implies that the error signal ϵ_j is proportional to the current model flux error along the vector $\mathbf{J}\,\hat{\boldsymbol{u}}^a$. Hence, the flux adaptation law is formulated along this vector, depicted in Fig. 3, as

$$\hat{\boldsymbol{\lambda}}^{i}_{\hat{d}q} = \hat{\boldsymbol{\Lambda}}_{dq}(\boldsymbol{i}_{\hat{d}q}) + \mathbf{J}\,\hat{\boldsymbol{u}}^a \cdot k'_j \int \epsilon_j \,\mathrm{d}t \tag{39}$$

where $k'_j = |\hat{\boldsymbol{\lambda}}^{a}_{\hat{d}q0}|\, k_j$ is the integral gain.

In steady-state, the adaptation (39) mitigates the current model flux error along the vector $\mathbf{J}\,\hat{\boldsymbol{u}}^a$. Consequently, the torque estimation error in (35) converges to zero and accurate torque control becomes realizable. It is worth pointing out that the steady-state position error remains unaffected by the flux adaptation. It can also be shown that the flux estimation error in (15) converges to zero under adaptation.

E. Susceptibility to Stator Resistance

In the presence of stator resistance error, the steady-state error in flux and torque estimation is inevitable. The flux adaptation converges to an inaccurate value that is given by

$$\begin{aligned} \epsilon_j =& \left(\mathbf{J}\,\boldsymbol{\phi}_\theta\right)^{\mathrm{T}} \boldsymbol{H}_{\tilde{\boldsymbol{\lambda}}^i}\, \tilde{\boldsymbol{\lambda}}^{i}_{\hat{d}q0} + \left(\mathbf{J}\,\boldsymbol{\phi}_\theta\right)^{\mathrm{T}} \boldsymbol{h}_{\tilde{R}}\, \tilde{R}_s = 0 \\ \Rightarrow & \left(\mathbf{J}\,\hat{\boldsymbol{u}}^a\right)^{\mathrm{T}} \cdot \tilde{\boldsymbol{\lambda}}^{i}_{\hat{d}q0} = \frac{1}{\omega_0} \left(\hat{\boldsymbol{u}}^a\right)^{\mathrm{T}} \boldsymbol{i}_{\hat{d}q0} \cdot \tilde{R}_s. \end{aligned} \tag{40}$$

Thus, the resistance error introduces a steady-state current model flux error orthogonal to the auxiliary flux vector. Owing to the inverse relation with the angular speed, the influence of stator resistance diminishes at high speeds.

Finally, using (40) in (35), the steady-state torque estimation error due to the resistance error is given by

$$\tilde{T}_0 = \frac{3p}{2}\, \boldsymbol{i}^{\mathrm{T}}_{\hat{d}q0}\, \mathbf{J}\, (\boldsymbol{G} + \omega_0 \mathbf{J})^{-1} \left[\boldsymbol{G}\, \mathbf{J}\hat{\boldsymbol{u}}^a\, \frac{\left(\hat{\boldsymbol{u}}^a\right)^{\mathrm{T}} \boldsymbol{i}_{\hat{d}q0}}{\omega_0} - \boldsymbol{i}_{\hat{d}q0} \right] \cdot \tilde{R}_s. \tag{41}$$

The steady-state torque estimation error contour for $\tilde{R}_s = 1\Omega$ (0.16 p.u.) at $\omega = 0.2$ p.u. (300 rpm) and $\omega = 0.8$ p.u. (1200 rpm) is shown in Figs. 8(a) and 8(b), respectively. The torque estimation error due to imprecise resistance is observed to increase with the stator current magnitude and decrease with the angular speed.

V. Stability Analysis

The error dynamics of the position observer in (22) can be expressed using the observed speed error $\tilde{\omega}_i = \omega - \hat{\omega}$ as

$$s\,\tilde{\theta} = \tilde{\omega}_i - k_p\,\epsilon_\theta \qquad s\,\tilde{\omega}_i = -k_i\,\epsilon_\theta. \tag{42}$$

It follows from (39) that the current model flux error dynamics with adaptation along $\mathbf{J}\,\hat{\boldsymbol{u}}^a$ become

$$\left(\mathbf{J}\hat{\boldsymbol{u}}^a\right)^{\mathrm{T}} s\tilde{\boldsymbol{\lambda}}^{i}_{\hat{d}q} = -k'_j\,\epsilon_j. \tag{43}$$

Using the flux estimation error dynamics (15) and the error signal dynamics (17), the small signal stability is analyzed as

$$s\,\boldsymbol{x} = \boldsymbol{A}\,\boldsymbol{x} \tag{44}$$

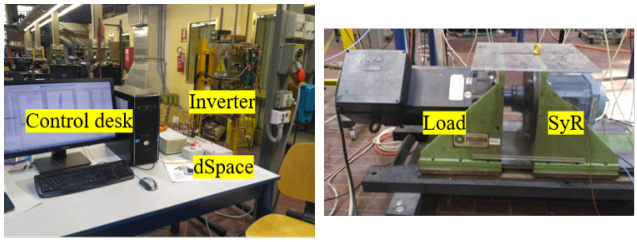

Fig. 10. Experimental Setup of 1.1 kW SyR motor under test on a dSPACE DS1103 control platform at a sampling frequency of 10 kHz.

TABLE I
MOTOR PARAMETERS

Parameters	Symbol	Values	Units
Rated power	P_n	1.1	kW
Rated voltage	V_n	340	V
Rated speed	ω_n	1500	rpm
Rated current	I_n	2.3	A
Rated torque	T_n	7.1	Nm
Pole pairs	p	2	-
Stator resistance	R_s	6.8	Ω
Shaft inertia	J	0.04	kgm^2

where $\boldsymbol{x} = \left[\left(\tilde{\boldsymbol{\lambda}}_{\hat{d}\hat{q}}\right)^{\mathrm{T}} \quad \tilde{\theta} \quad \tilde{\omega}_i \quad \left(\mathbf{J}\hat{\boldsymbol{u}}^a\right)^{\mathrm{T}}\tilde{\boldsymbol{\lambda}}^i_{\hat{d}\hat{q}}\right]^{\mathrm{T}}$ and $\boldsymbol{A} =$

$$\begin{bmatrix} -(\boldsymbol{G}+\omega_0\,\mathbf{J}) & \boldsymbol{G}\,\hat{\boldsymbol{\lambda}}^a_{\hat{d}\hat{q}0} & \mathbf{0} & \boldsymbol{G}\,\mathbf{J}\,\hat{\boldsymbol{u}}^a \\ k_p\,\boldsymbol{\phi}_\theta^{\mathrm{T}} & -k_p\,\boldsymbol{\phi}_\theta^{\mathrm{T}}\,\hat{\boldsymbol{\lambda}}^a_{\hat{d}\hat{q}0} & 1 & -k_p\,\boldsymbol{\phi}_\theta^{\mathrm{T}}\,\mathbf{J}\,\hat{\boldsymbol{u}}^a \\ k_i\,\boldsymbol{\phi}_\theta^{\mathrm{T}} & -k_i\,\boldsymbol{\phi}_\theta^{\mathrm{T}}\,\hat{\boldsymbol{\lambda}}^a_{\hat{d}\hat{q}0} & 0 & -k_i\,\boldsymbol{\phi}_\theta^{\mathrm{T}}\,\mathbf{J}\,\hat{\boldsymbol{u}}^a \\ k'_j\left(\mathbf{J}\,\boldsymbol{\phi}_\theta\right)^{\mathrm{T}} & -k'_j\left(\mathbf{J}\,\boldsymbol{\phi}_\theta\right)^{\mathrm{T}}\hat{\boldsymbol{\lambda}}^a_{\hat{d}\hat{q}0} & 0 & -k'_j\left(\mathbf{J}\,\boldsymbol{\phi}_\theta\right)^{\mathrm{T}}\mathbf{J}\,\hat{\boldsymbol{u}}^a \end{bmatrix}. \tag{45}$$

The gains of the PLL are chosen for a critically damped response (23) with the poles at $s = -\Omega_\omega = -2\,\pi\cdot 25$ rad/s. The flux observer gain is set to 0.2 p.u. of rated speed as $g = 2\,\pi\cdot 10$ rad/s. The gain of current model flux adaptation is $k_j = 2\,\pi\cdot 4$ rad/s.

Fig. 9 shows the eigenvalues of (44) for $\omega = 0.1\ldots 1$ p.u. at rated torque $T = 7.1$ Nm on MTPA trajectory. The closed loop poles of the combined dynamics of the proposed control system are observed to be stable.

VI. EXPERIMENTAL RESULTS

The proposed torque control scheme with current model flux adaptation is validated experimentally with a 1.1 kW SyR motor on a dSPACE DS1103 control platform running at a sampling frequency of 10 kHz. A picture of the setup is shown in Fig. 10. The parameters of the SyR motor under test are tabulated in Table I.

The SyR machine operates in the torque control mode and the auxiliary drive in the speed control mode. A minimum stator current $i_{d,min} = 1$ A is imposed for fundamental excitation at no load. The incremental inductance matrix $\hat{\boldsymbol{L}}_\partial$ is computed in real-time from the flux-map; as an example:

$$\hat{l}_d(\boldsymbol{i}_{dq}) = \frac{\hat{\boldsymbol{\Lambda}}_d(i_d+\delta i_d, i_q) - \hat{\boldsymbol{\Lambda}}_d(i_d, i_q)}{\delta i_d} \tag{46}$$

where δi_d is a small value (≈ 10 mA). The other incremental inductances are computed in a similar fashion. Note that in

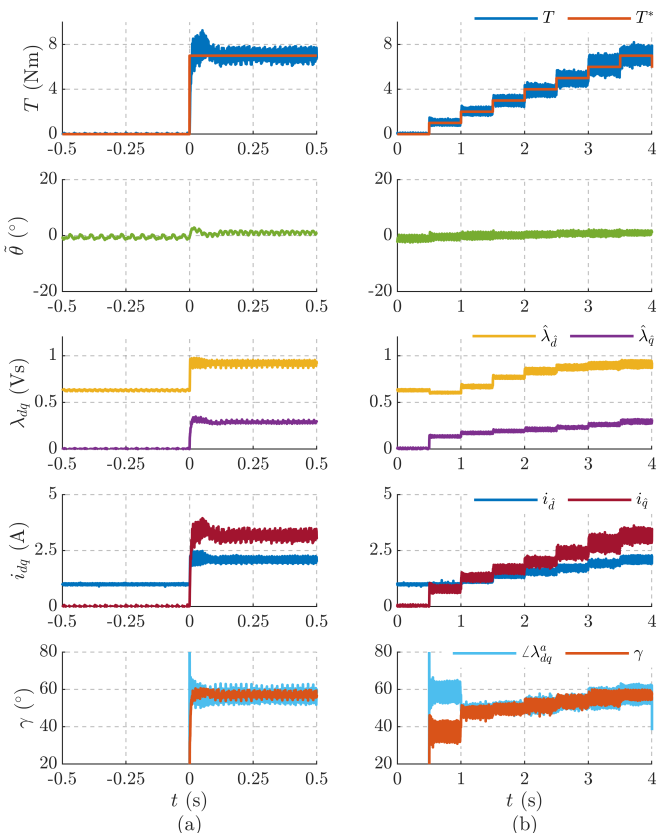

Fig. 11. Optimal torque control of the proposed scheme at rated speed $\omega = 1$ p.u. (1500 rpm): (a) Rated torque step $T^* = 0 \rightarrow 7.1$ Nm at $t = 0$ s; (b) Incremental torque reference.

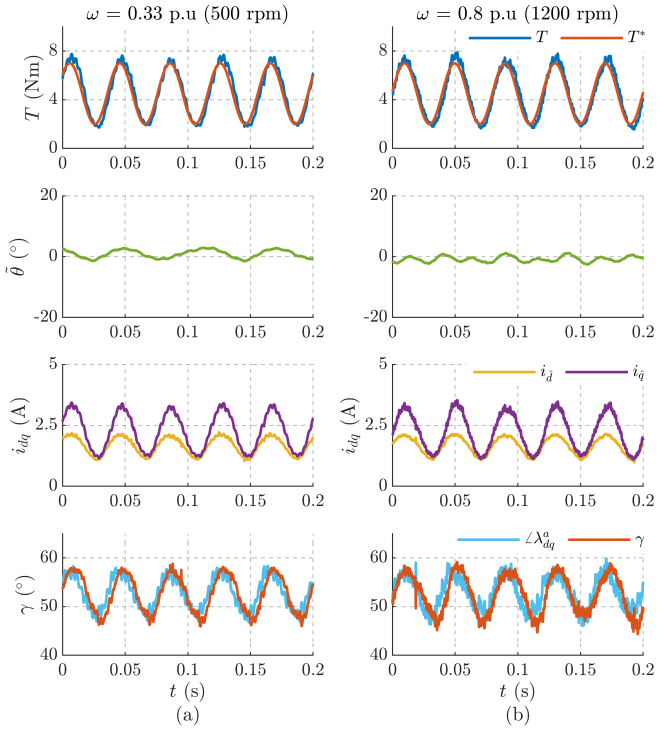

Fig. 12. Dynamic MTPA adaptation with sinusoidal torque reference (25 Hz). Operating speed: (a) $\omega = 0.33$ p.u. (500 rpm); (b) $\omega = 0.8$ p.u. (1200 rpm).

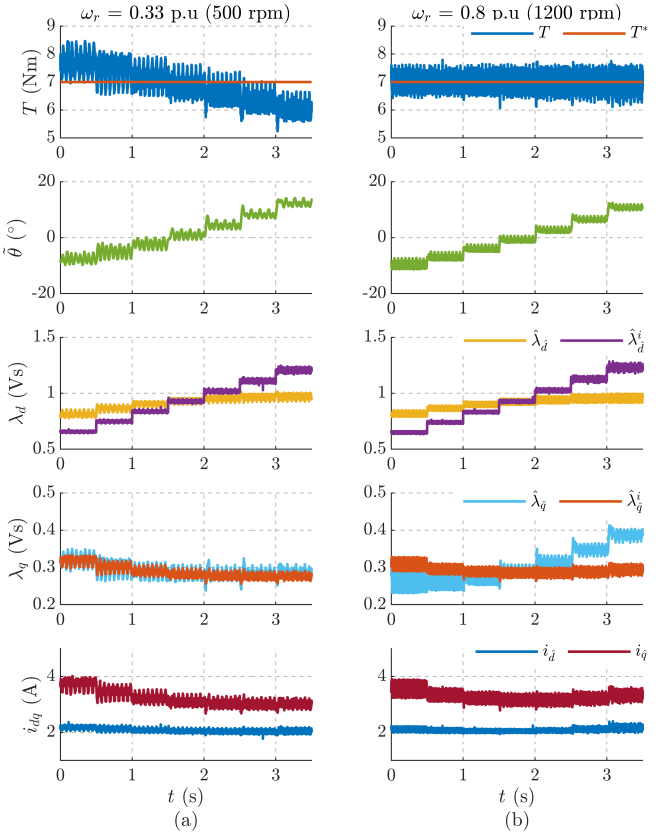

Fig. 13. Torque control at $T^* = 7.1$ Nm under parameter error in d-axis varying from +30% ($\hat{\lambda}^i_d = 0.7\,\lambda_d$) to -30% ($\hat{\lambda}^i_d = 1.3\,\lambda_d$) in steps of -10% increment every 0.5 s. Operating speed: (a) $\omega = 0.33$ p.u. (500 rpm); (b) $\omega = 0.8$ p.u. (1200 rpm).

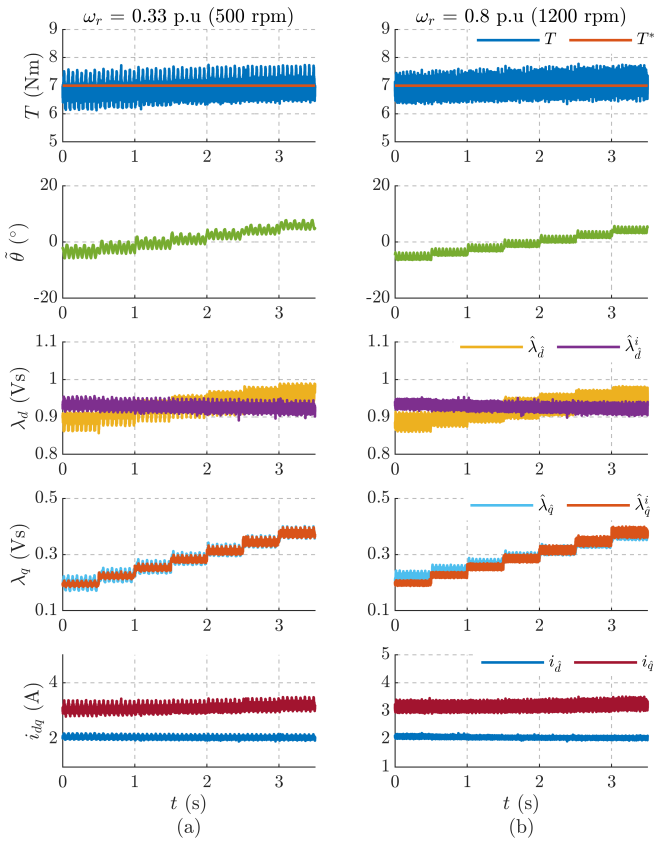

Fig. 14. Torque control at $T^* = 7.1$ Nm under parameter error in q-axis varying from +30% ($\hat{\lambda}^i_q = 0.7\,\lambda_q$) to -30% ($\hat{\lambda}^i_q = 1.3\,\lambda_q$) in steps of -10% increment every 0.5 s. Operating speed: (a) $\omega = 0.33$ p.u. (500 rpm); (b) $\omega = 0.8$ p.u. (1200 rpm).

the following results, the quantity T, representing the real torque, is computed from the accurate reference flux-map and the position acquired using an encoder.

A. Optimal Torque Control

The proposed torque control scheme is validated at rated speed with a rated torque step $T^* = 0 \rightarrow 7.1$ Nm at $t = 0$ s in Fig. 11(a). The control is stable with small transient position error ($< 5°$) and is observed to track the torque step reference seamlessly.

In the second test, the torque reference is commanded in small incremental steps at the rated speed, shown in Fig. 11(b). For small loads ($t < 1$ s), the MTPA condition is not respected due to the imposition of minimum stator current. For higher loads ($t > 1$ s), the current angle is shown to be coincident with the phase of auxiliary flux vector for MTPA operation, i.e., $\gamma = \angle \boldsymbol{\lambda}^a_{dq}$.

The dynamic capability of the proposed torque control to track MTPA is evaluated with a sinusoidal torque reference at 25 Hz in Fig. 12 at two different speeds; the current angle is observed to track the phase of auxiliary flux vector. The use of analytical formulation to attain the MTPA state without an additional regulator facilitates the dynamic tracking of MTPA.

B. Operation under Parameter Errors

The susceptibility of torque controller and position observer in the presence of parameter error in d-axis without flux adaptation is demonstrated in Fig. 13. A varying error from +30% ($\hat{\lambda}^i_d = 0.7\,\lambda_d$) to -30% ($\hat{\lambda}^i_d = 1.3\,\lambda_d$) is imposed in steps of -10% increment at rated torque reference $T^* = 7.1$ Nm and rotor speeds $\omega = 0.33$ p.u. (500 rpm) and $\omega = 0.8$ p.u. (1200 rpm) in Figs. 13(a) and 13(b), respectively. Higher speeds are not feasible at rated torque due to voltage limitation as the control diverges from the optimal MTPA point under parameter error.

The maximum position error is observed to be $\tilde{\theta}_0 \approx 15°$, drawing correlation to the steady-state position error (26) in Fig. 4(a). It can be discerned from Fig. 13 that the position error is independent of operating speed. On contrary, the torque estimation error is more prominent at low speed in Fig. 13(a) where, at $t < 0.5$ s, it is approximately -0.75 Nm (-10%) for +30% d-axis flux error, in accordance with the analytical evaluation in Fig. 6(a). The torque error is diminished at high speed in Fig. 13(b), as evaluated in Fig. 6(b).

A similar test is conducted for varying errors in the q-axis flux-map in Fig. 14. The speed-independent steady-state position error is observed to be $\tilde{\theta}_0 < 5°$, supporting the analysis in Fig. 4(b). The torque estimation shows more resilience towards parameter error in q-axis, in accordance with Fig. 7.

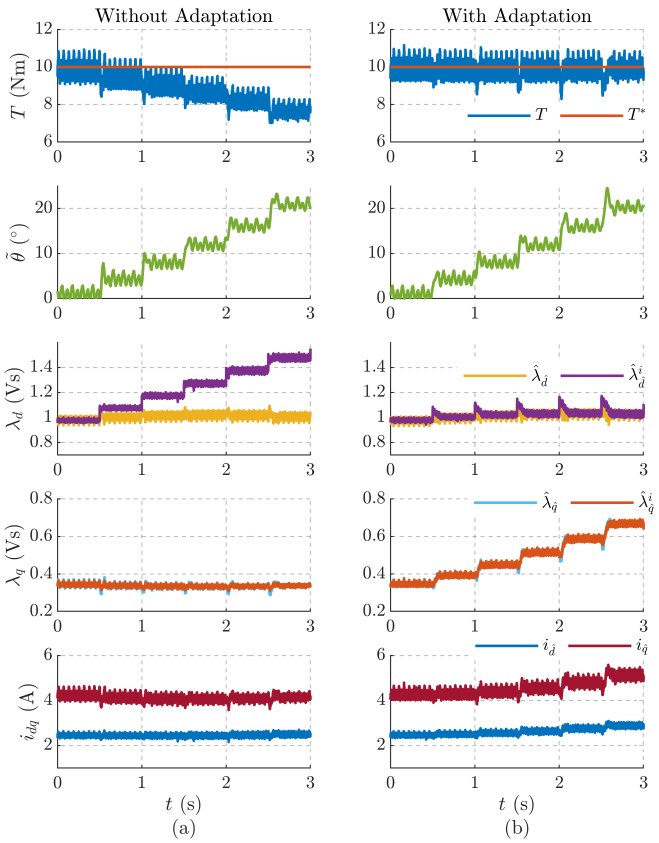

Fig. 15. Torque control at $T^* = 1.4$ p.u. (10 Nm) and $\omega = 0.33$ p.u. (500 rpm) under parameter error in d-axis varying from 0% to -50% ($\hat{\lambda}^i_d = 1.5\,\lambda_d$) in steps of -10% increment every 0.5 s: (a) Without flux adaptation; (b) With flux adaptation.

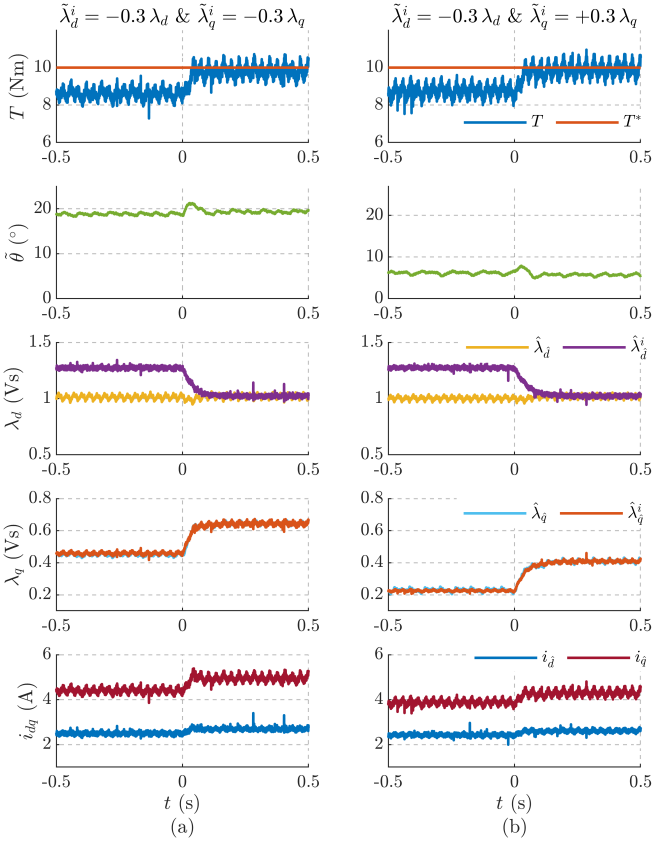

Fig. 16. Flux adaptation enabled at $t = 0$ s in the torque control at $T^* = 1.4$ p.u (10 Nm) and $\omega = 0.33$ p.u. (500 rpm) under parameter errors in both axes: (a) -30% in d-axis ($\hat{\lambda}^i_d = 1.3\,\lambda_d$) and -30% in q-axis ($\hat{\lambda}^i_q = 1.3\,\lambda_q$); (b) -30% error in d-axis and +30% error in q-axis ($\hat{\lambda}^i_q = 0.7\,\lambda_q$).

C. Current Model Flux Adaptation

The efficacy of the current model flux adaptation is demonstrated at $\omega = 0.33$ p.u. (500 rpm) and at 40% overload in torque $T^* = 1.4$ p.u. (10 Nm) with a varying error in the d-axis flux-map from zero to -50% ($\hat{\lambda}^i_d = 1.5\,\lambda_d$) in steps of -10% increment every 0.5 s, as shown in Fig. 15. The performance of the control without and with the flux adaptation is juxtaposed in Figs. 15(a) and 15(b), respectively. A maximum torque error of +24% is observed in Fig. 15(a) while in Fig. 15(b), accurate torque control is observed despite the high position error.

The dynamics of the current model flux adaptation is illustrated in Fig. 16 at $T^* = 1.4$ p.u. (10 Nm) and $\omega = 0.33$ p.u. (500 rpm) where the adaptation is enabled at $t = 0$ s. Fig. 16(a) considers a -30% flux-map error in either axes while Fig. 16 has -30% error in d-axis and +30% error in q-axis. For $t < 0$ s, the torque error is approximately 15% in both the figures as it is dominated by the d-axis error. Conversely, the q-axis flux-map error has a substantial influence on the position error; hence, a high error $\tilde{\theta} \approx 19°$ is discerned in Fig. 16(a) while it is reduced in Fig.16(b) where the flux-map errors carry opposite signs.

Once the adaptation is enabled at $t = 0$ s, the observed and current model flux quantities converge and accurate torque is realized. It is worth highlighting that the position error remains unaltered by the flux adaptation due to the orthogonality of projection vectors. Moreover, the stator flux and currents in estimated reference frame settle at different values in the two figures due to the different position errors.

D. Susceptibility to Stator Resistance

The susceptibility of the proposed torque control scheme to a stator resistance perturbation of $\tilde{R}_s = \pm 1\Omega$ (0.16 p.u.) is evaluated at speeds $\omega = 0.2$ p.u. (300 rpm) and $\omega = 0.8$ p.u. (1200 rpm) in Figs. 17(a) and 17(b), respectively. In accordance to the analytical estimate in Fig. 8, the maximum torque error is approximately 0.8 Nm at 300 rpm and less than 0.2 Nm at 1200 rpm. It is worth pointing out that the position error is null despite the variations in stator flux and torque, attesting to the resistance immunity property of the APP scheme.

VII. Conclusion

This paper proposed a torque control scheme for sensorless synchronous motor drives with model-based optimal reference generation for MTPA tracking. Following the linearized error dynamics of flux observer, a comprehensive error signal is expressed as a function of position error, resistance error and current model flux error in a projection vector framework. A position observer based on the adaptive projection vector for

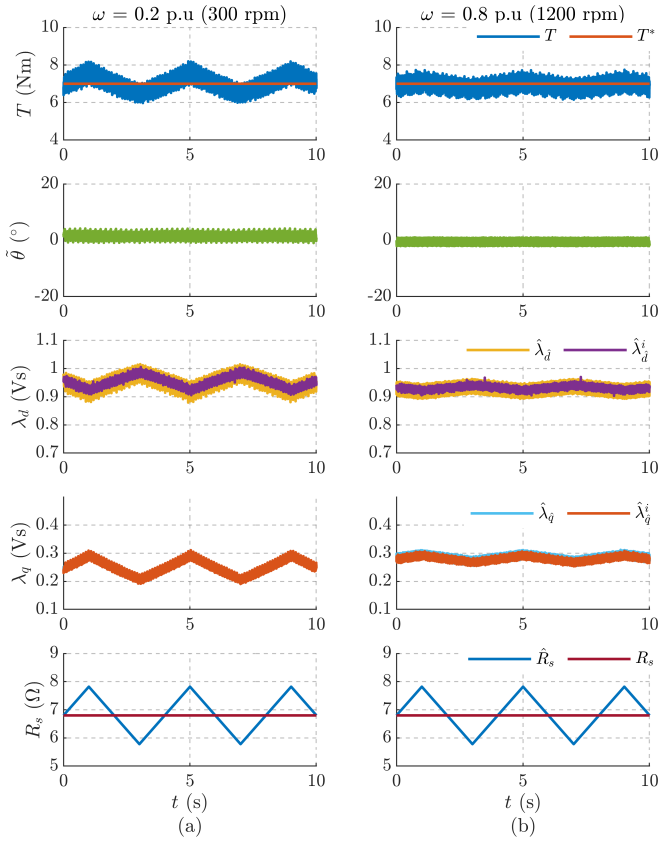

Fig. 17. Susceptibility of the proposed torque control to a stator resistance perturbation of $\tilde{R}_s = \pm 1\Omega$ (0.16 p.u.) at rated torque: (a) $\omega = 0.2$ p.u. (300 rpm); (b) $\omega = 0.8$ p.u. (1200 rpm).

position error estimation is designed, possessing immunity to resistance error on MTPA trajectory.

The MTPA criterion is analytically shown to hold when the current vector is in phase with the auxiliary flux vector. Using the discrepancy in estimated and commanded torque, a model-based optimal reference is generated, respecting the current limits. Thus, the accuracy of torque control is directly coupled to the accuracy of torque estimation.

Exploiting the additional degree of freedom, the orthogonal projection vector to APP is used for current model flux error adaptation. It has been shown that the flux adaptation mitigates error in torque estimation; consequently, the accurate torque control becomes realizable. Moreover, due to orthogonality, the position observer is decoupled from the flux adaptation.

The performance of the proposed torque control sensorless scheme with adaptation under parameter errors is experimentally validated on a 1.1 kW SyR machine test bench.

REFERENCES

[1] P. L. Jansen and R. D. Lorenz, "Transducerless position and velocity estimation in induction and salient AC machines," *IEEE Transactions on Industry Applications*, vol. 31, no. 2, pp. 240–247, 1995.

[2] C. E. Hwang, Y. Lee, and S. K. Sul, "Analysis on position estimation error in position-sensorless operation of IPMSM using pulsating square wave signal injection," *IEEE Transactions on Industry Applications*, vol. 55, no. 1, pp. 458–470, 2019.

[3] R. Morales-Caporal and M. Pacas, "Suppression of saturation effects in a sensorless predictive controlled synchronous reluctance machine based on voltage space phasor injections," *IEEE Transactions on Industrial Electronics*, vol. 58, no. 7, pp. 2809–2817, jul 2011.

[4] A. Piippo, M. Hinkkanen, and J. Luomi, "Sensorless control of PMSM drives using a combination of voltage model and HF signal injection," in *Conference Record - IAS Annual Meeting (IEEE Industry Applications Society)*, vol. 2, 2004, pp. 964–970.

[5] A. Varatharajan, P. Pescetto, and G. Pellegrino, "Sensorless Synchronous Reluctance Motor Drives: A Full-Speed Scheme using Finite-Control-Set MPC in a Projection Vector Framework," *IEEE Transactions on Industry Applications*, vol. 56, no. 4, pp. 3809–3818, 2020.

[6] M. Hinkkanen, T. Tuovinen, L. Harnefors, and J. Luomi, "A Combined Position and Stator-Resistance Observer for Salient PMSM Drives: Design and Stability Analysis," *IEEE Transactions on Power Electronics*, vol. 27, no. 2, pp. 601–609, 2012.

[7] Y. Lee and S. K. Sul, "Model-Based Sensorless Control of an IPMSM With Enhanced Robustness Against Load Disturbances Based on Position and Speed Estimator Using a Speed Error," *IEEE Transactions on Industry Applications*, vol. 54, no. 2, pp. 1448–1459, 2018.

[8] I. Boldea, M. C. Paicu, G. Andreescu, and F. Blaabjerg, ""Active Flux" DTFC-SVM Sensorless Control of IPMSM," *IEEE Transactions on Energy Conversion*, vol. 24, no. 2, pp. 314–322, 2009.

[9] S. C. Agarlita, I. Boldea, and F. Blaabjerg, "High-frequency-injection-assisted 'active-flux'-based sensorless vector control of reluctance synchronous motors, with experiments from zero speed," *IEEE Transactions on Industry Applications*, vol. 48, no. 6, pp. 1931–1939, 2012.

[10] M. Hinkkanen, S. E. Saarakkala, H. A. A. Awan, E. Mölsä, and T. Tuovinen, "Observers for Sensorless Synchronous Motor Drives: Framework for Design and Analysis," *IEEE Transactions on Industry Applications*, vol. 54, no. 6, pp. 6090–6100, 2018.

[11] A. Yousefi-Talouki, P. Pescetto, G. Pellegrino, and I. Boldea, "Combined Active Flux and High-Frequency Injection Methods for Sensorless Direct-Flux Vector Control of Synchronous Reluctance Machines," *IEEE Transactions on Power Electronics*, vol. 33, no. 3, pp. 2447–2457, 2018.

[12] A. Varatharajan and G. Pellegrino, "Sensorless Synchronous Reluctance Motor Drives: A General Adaptive Projection Vector Approach for Position Estimation," *IEEE Transactions on Industry Applications*, pp. 1–10, 2019.

[13] ——, "Sensorless Synchronous Reluctance Motor Drives: A Projection Vector Approach for Stator Resistance Immunity and Parameter Adaptation," *IEEE Transactions on Industry Applications*, pp. 1–10, 2020.

[14] J. Yoo, Y. Lee, and S. K. Sul, "Back-EMF Based Sensorless Control of IPMSM with Enhanced Torque Accuracy Against Parameter Variation," in *2018 IEEE Energy Conversion Congress and Exposition (ECCE)*, 2018, pp. 3463–3469.

[15] E. Armando, R. I. Bojoi, P. Guglielmi, G. Pellegrino, and M. Pastorelli, "Experimental identification of the magnetic model of synchronous machines," *IEEE Transactions on Industry Applications*, vol. 49, no. 5, pp. 2116–2125, 2013.